Eur. Phys. J. B (2015)
DOI: 10.1140/epjb/e2015-60227-x

THE EUROPEAN PHYSICAL JOURNAL B

Regular Article

Temperature-induced phase transformation of $Fe_{1-x}Ni_x$ alloys: molecular-dynamics approach

Emilia Sak-Saracino and Herbert M. Urbassek[a]

Physics Department and Research Center OPTIMAS, University Kaiserslautern, Erwin-Schrödinger-Straße, 67663 Kaiserslautern, Germany

Received 21 March 2015 / Received in final form 8 May 2015
Published online (Inserted Later) – © EDP Sciences, Società Italiana di Fisica, Springer-Verlag 2015

Abstract. Using molecular-dynamics simulation, we study the temperature induced bcc/fcc phase transformation of random $Fe_{1-x}Ni_x$ alloys in the concentration range of $x \leq 40$ at%. The Meyer-Entel potential describes faithfully the decrease of the transition temperature with increasing Ni concentration. The austenite transformation proceeds by homogeneous nucleation and results in a fine-grained poly-crystalline structure. The transformation follows the Nishiyama-Wassermann orientation relationship. The martensite phase nucleates at the grain boundaries (heterogeneous nucleation). Even for the largest crystallite studied (2.75×10^5 atoms) the back-transformation results in a single-crystalline grain containing only a small amount of defects. The morphological changes in the transformed material show no significant dependence on Ni content.

1 Introduction

$Fe_{1-x}Ni_x$ alloys are completely miscible at temperatures between 1183 and 1665 K, where they exhibit the fcc crystal structure. At low temperatures, Fe-rich crystals show the bcc structure, at $x \sim 0.75$, the ordered intermetallic compound $FeNi_3$ with $L1_2$ structure is stable, while Ni-rich crystals remain in the fcc phase [1]. Besides their role for magnetic applications, $Fe_{1-x}Ni_x$ alloys are renowned for their Invar properties [1].

The martensitic transformation occurring when an Fe-rich high-temperature crystal is quickly cooled down has been extensively studied [1,2]. Experimentally the transformation is found up to a maximum Ni concentration of $x = 0.34$, which coincides with the structurally stable Invar concentration. Due to the importance of this material, the transformation has been modeled repeatedly. Atomistic simulation based on molecular dynamics was early used to study this transformation. Yu and Clapp [3] constructed a volume-dependent interaction potential and used it to set up a biphasic system and study the migration of the fcc/bcc interface. Grujicic et al. [4,5] created their own potential to describe the transformation; they concluded that the martensitic transformation requires defects to occur. The orientation relationship followed neither the well-known patterns of Kurdjumov-Sachs (KS) [6] nor of Nishiyama-Wassermann (NW) [7,8], presumably because the orientation of their simulation box was incompatible with either of these relationships. Another potential was provided by Meyer and Entel [9] who studied the transformation in a series of papers [9–12]. This potential belongs to the embedded-atom-model (EAM) class. These authors calculated the martensite-austenite transition temperature as a function of the Ni concentration and found it in good agreement with experiment [2]. They found that the transformation follows orientation relationships closely related to NW. In addition they studied the phonon dispersion relations of the alloy.

The Meyer-Entel potential was also used to describe the phase transformation behavior of FeNi nanoparticles [13–16] and to discuss – among other features – the dependence of the transformation temperature on the nanoparticle size. The transformation behavior differs from bulk material in that the free surfaces in the nanoparticles provide nucleation sites for heterogeneous nucleation. Thus for, example, Kar'kina et al. [16] found that the occurrence and characteristics of the austenitic phase transformation depends sensitively on the cluster size in the size regime of $N = 55$–2869 atoms.

Later several further potentials were created to describe the $Fe_{1-x}Ni_x$ system; these were primarily motivated by the importance of this system for steel. The EAM potential created by Bonny et al. [17] allows to model the system at low temperatures, where it correctly predicts the change of bcc via $L1_2$ to fcc structures with increasing x; however, since a stable high-temperature Fe fcc phase is missing, this potential does not allow to model the temperature-induced bcc → fcc transformation. Similarly the work of Mishin et al. [18] is aimed at the low-temperature description of the system. These authors provide an EAM potential augmented by bond-angle terms (the so-called angular dependent potential, ADP) to take the covalent component of bonding that exists in FeNi

[a] e-mail: urbassek@rhrk.uni-kl.de

into account. This potential is able to describe the stable ordered phases existing in this system. Recently, Malerba et al. [19] presented the so-called JMR potential to specifically model austenitic alloys. It is an EAM potential based on ab-initio calculations on the density-functional-theory level.

In the present paper we take up the task of characterizing the austenitic/martensitic transformation in $Fe_{1-x}Ni_x$ systems. We use the established Meyer-Entel potential [9] but go beyond previous work by Entel et al. [9,20–22] by studying larger systems; this allows us to obtain detailed information on the nucleation process of the new phase. Thus we show that the phase nucleation process proceeds differently in the larger systems than in the smaller systems studied up to now. In particular we demonstrate that the austenitic transformation of a bulk single-crystalline sample occurs by the homogeneous nucleation of several cp grains in the bcc matrix while the martensitic transformation proceeds by the heterogeneous nucleation of the bcc phase at the grain boundaries. This asymmetry in the bcc-fcc phase transformation of an Fe-based alloy is shown here for the first time in a large simulation volume.

2 Simulation method

We use the method of classical molecular dynamics (MD) simulation to study the α-γ phase transition in $Fe_{1-x}Ni_x$ alloys. The simulation volume is set up as a cube and contains a bcc crystallite with {100} surfaces. Periodic boundary conditions are employed in all three directions. We study two systems: a small system consisting of around 2000 atoms with dimensions $28.72 \times 28.72 \times 28.72$ Å^3 – corresponding to 10 atom layers in all ⟨100⟩ directions – and a large system containing around 275 000 atoms; here the dimensions are $142.78 \times 142.78 \times 142.78$ Å^3 corresponding to 50 atom layers in each direction.

The systems consist of Fe atoms, in which Ni atoms are inserted randomly on substitutional sites. Five Ni atom concentrations are studied: $x = 0$, 10, 20, 30, and 40 at%. For each concentration, 5 different random crystals are set up; the results reported below are averages over these 5 systems. The interactions in this system are described by the Meyer-Entel interaction potential [9].

To start the simulation, the system is relaxed at a temperature of 0 K to reduce the pressure to zero; pressure control is applied in all three directions independently such that the simulation volume can deform to a cuboid with unequal axes.

After relaxation, a heating/cooling cycle is applied, in which the temperature is increased from 0 K up to 1200 K with a heating rate of 1 K/ps and then analogously cooled down. During the cycle again three-axial pressure control is applied to keep the pressure in all directions at 0 GPa. The austenite and martensite temperatures are determined from the volume-temperature hysteresis (see Fig. 2 below).

All calculations are performed with the open-source LAMMPS code [23] and the local atomic structure is analyzed using common-neighbor analysis (CNA) [24].

Table 1. (a) Cohesive energy (eV) at 0 K and (b) lattice constants (Å) at 300 K for elemental Fe and Ni for the Meyer-Entel [9] potential, compared to reference data obtained by experiment and ab-initio calculations.

(a)

	Fe		Ni	
	bcc	fcc	bcc	fcc
Meyer-Entel	4.278	4.241	4.395	4.451
Reference data	4.28[a]	4.15–4.21[b]	4.36[c,d]	4.45[d]

[a]Reference [25], [b]depending on antiferromagnetic structure, reference [18]. [c]Reference [26]. [d]Reference [27].

(b)

	Fe		Ni	
	bcc	fcc	bcc	fcc
Meyer-Entel	2.869	3.686	2.819	3.519
Reference data	2.866[a,b]	3.571[b]	2.801[c]	3.52[a]

[a]Reference [25]. [b]Reference [1]. [c]Reference [18].

3 Results

Table 1 summarizes basic information about the performance of the Meyer-Entel potential for the pure elements, Fe and Ni, in fcc and bcc phase. For the determination of the properties of the metastable phases (low-temperature fcc-Fe and bcc-Ni), ab-initio data are included [18]. However the prediction of the lattice constant of fcc-Fe using spin-polarized LAPW/GGA calculations gives rather small values of the fcc-Fe lattice constant: 3.430–3.483 Å, depending on the antiferromagnetic structure [18]. Here we use experimental data obtained from extrapolating measured data for fcc-FeC (and fcc-FeN) alloys to zero C (and N) concentration ([1], Tab. 1.3). We see overall fair agreement between the data predicted by the Meyer-Entel potential and the reference data. Note that the Ni atom is smaller than the Fe atom both in the bcc and in the fcc phase.

The performance of the Meyer-Entel potential for describing the $Fe_{1-x}Ni_x$ system has been checked by the authors of this potential [9]. They calculated the energy difference between the fcc and bcc phase and found that at 0 K, the bcc phase is stable up to almost $x = 50$ at% [22]. We add in Figure 1 information about the dependence of the lattice constant of the $Fe_{1-x}Ni_x$ alloys on Ni content at 300 K. To obtain reliable values, the lengths of all cuboid sides were averaged; in addition the data was taken as a mean value over a time period of 150 ps. From Figure 1 we conclude that the lattice constants as obtained for the Meyer-Entel potential are in good agreement with available experimental data [28–30], both for the bcc and the fcc structure.

3.1 Austenitic and martensitic transition temperatures

We study two system sizes, one with 2×10^3 and one with around 2.75×10^5 atoms; this allows us to study

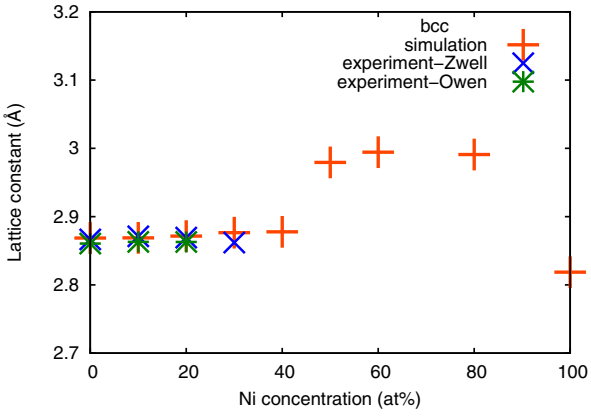

(a)

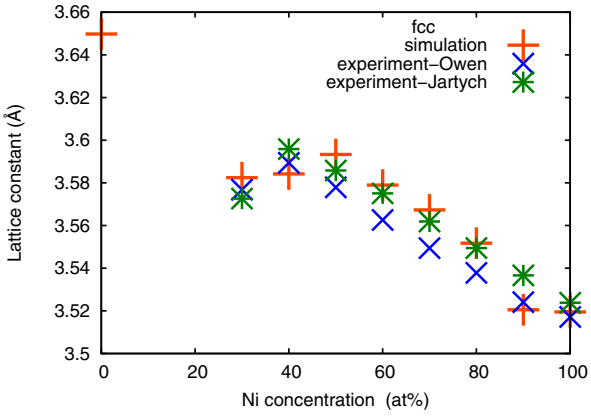

(b)

Fig. 1. Lattice constant of the (a) bcc and (b) fcc phases of $Fe_{1-x}Ni_x$ as a function of Ni concentration x at 0 K. Simulation data are compared to the experimental values of Owen et al. [28], Zwell et al. [29] and Jartych et al. [30].

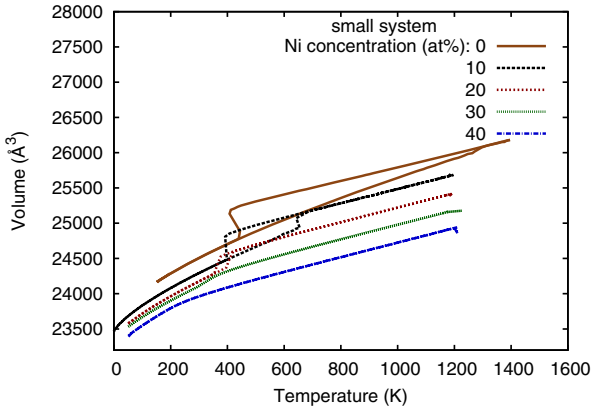

(a)

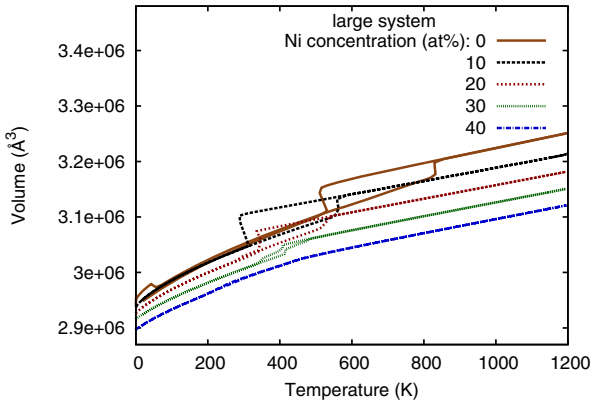

(b)

Fig. 2. Dependence of the system volume on temperature during the heating/cooling cycle for the (a) small system and the (b) large system for several values of the Ni concentration x.

the influence of system size on the phase transition behavior. Figure 2 shows the basic information obtained while our system is subjected to the heating/cooling cycle: the volume-temperature hysteresis curve. The temperatures at which the volume jumps are identified as the austenitic and martensitic transition temperatures. Note that with increasing Ni content x the volume jumps decrease in size and tend to smear out in temperature, until at $x = 40$ at% no transition is visible; this is a sign that the energy difference between fcc and bcc phases becomes smaller with increasing x. Similar hystereses have been observed experimentally in metallic systems during the austenitic/martensitic phase transition [30–32].

While the general trends are similar for the small and the large system, quantitative details differ. This points at different phase nucleation mechanisms for the two systems and will be discussed in Section 3.2 below.

We obtain the austenitic and martensitic transformation temperatures from the temperature jumps visible in Figure 2. These data are displayed in Figure 3; to be specific, we took the start temperatures of the transformations. For higher Ni concentration x the volume jump becomes almost imperceptible; then we used also information from the atomistic phase analysis to determine the transition temperature.

Figure 3 compares our simulation results for the martensite and austenite temperature with experimental data [2]. When comparing experimental and simulation data it must be remembered that the equilibrium transition temperature of the Meyer-Entel potential for pure Fe – as determined from the equality of the free energies of the bcc and fcc phases – is only around 550 K [33], while it is 1185 K in reality. Therefore we compare the trends in the data. We observe a good agreement between the small and the large system, in particular for the austenite temperatures. The decrease of the austenite temperature with increasing x agrees in trend with experimental data, at least for small x. For larger x we obtain a smaller austenite temperature than in experiment; this is caused by the smaller transition temperature in the Meyer-Entel potential. Previous simulations by Entel et al. gave a quasi-linear decrease from 1100 K ($x = 10$ at%) to 600 K ($x = 30$ at%) [9]; these data are higher than ours, presumably due to the higher heating rate used there (3.3 K/ps). In a later paper [21], smaller

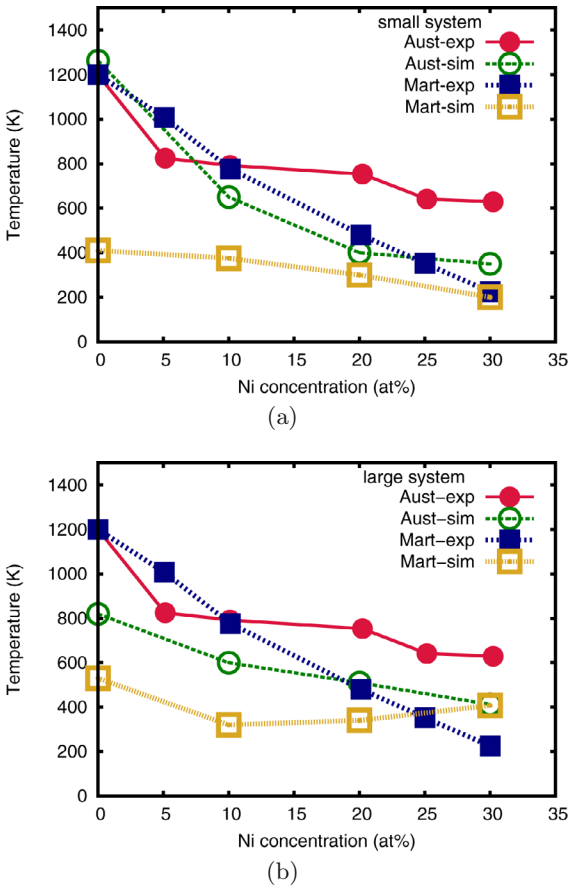

Fig. 3. Martensite and austenite start temperatures as a function of the Ni concentration x for the (a) small system and the (b) large system. Simulation results are compared to experimental data of Acet et al. [2].

values are reported – decreasing from 900 to 500 K for the Ni concentrations given above – which are more in line with ours.

The decrease of the austenite temperature with increasing Ni content x has been attributed to the increase of the magnetic pressure originating from antibonding $3d$ Ni electrons of minority spin stabilizing the fcc structure [20,22]. On the microscopic scale this leads to a softening of the bcc [110]-TA_1 phonons with increasing temperature such that the crystals become unstable against shear in [110] direction; this mechanism is operative equally for pure Fe [34] and for Fe-rich $Fe_{1-x}Ni_x$alloys [11,22].

Our martensite temperatures are rather unaffected by the Ni concentration x for the larger system, while they show a slowly decreasing trend with x for the smaller system. We assume these variations to be caused by the complex (heterogeneous) nucleation process of the martensite (see Fig. 6 and discussion in Sect. 3.2). Entel et al. [21] give even lower values, below 200 K, which also feature an unsystematic scatter with Ni content x. The small values may again be due to the faster cooling rate applied in their work; these authors also attribute the small values of the

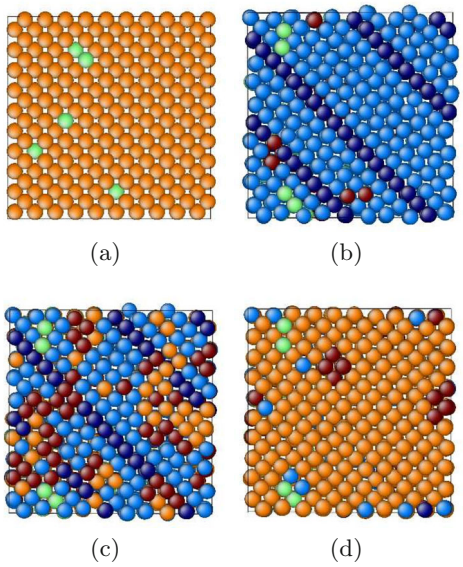

Fig. 4. Snapshots of the $Fe_{1-x}Ni_x$ crystallite (small system) with 10 at% Ni concentration (a) in the initial bcc structure and (b)–(d) during the martensitic transformation. Temperatures are (a) 0 K, (b) 390 K, (c) 380 K, (d) 375 K. The plotted plane corresponds to a bcc {100} plane. Colors denote the local crystal structure as obtained by CNA. Orange: bcc; dark blue: fcc; light blue: hcp; red: unknown; Ni atoms are green.

martensite temperatures (as compared to experiment) to the lack of including the bcc ferromagnetic properties into their potential.

3.2 Microstructure evolution during transformation

Figure 4 shows snapshots of the evolving microstructure during the phase transition in the small system. The initial bcc structure, Figure 4a, transforms at around 650 K to the austenitic structure. This structure remains stable during the ensuing heating and cooling process until a temperature of around 390 K is reached. It is displayed in Figure 4b and is characterized by a mixture of the two close-packed (cp) phases, hcp and fcc. In the Meyer-Entel potential, the energy difference between these two phases amounts to only 4.6 meV/atom [35]. The fcc {111} planes whose trace on the plotted planes are visible in Figure 4b are stacking faults in the hcp structure.

Figures 4c and 4d show the evolution of the structure through the martensitic transformation. It occurs in a narrow temperature window around 380 K. In Figure 4c, the first bcc embryos have nucleated; they appear at random places and feature the homogeneous nucleation of the new phase. After 5 ps, the transformation is essentially complete, Figure 4d. Note that the few unidentified atoms appearing in Figures 4b and 4d, caused by temperature fluctuations and local strains, have multiplied during the transformation itself (Fig. 4c).

Figure 5 shows a detailed study of the austenitic transformation in the large system for a Ni concentration of

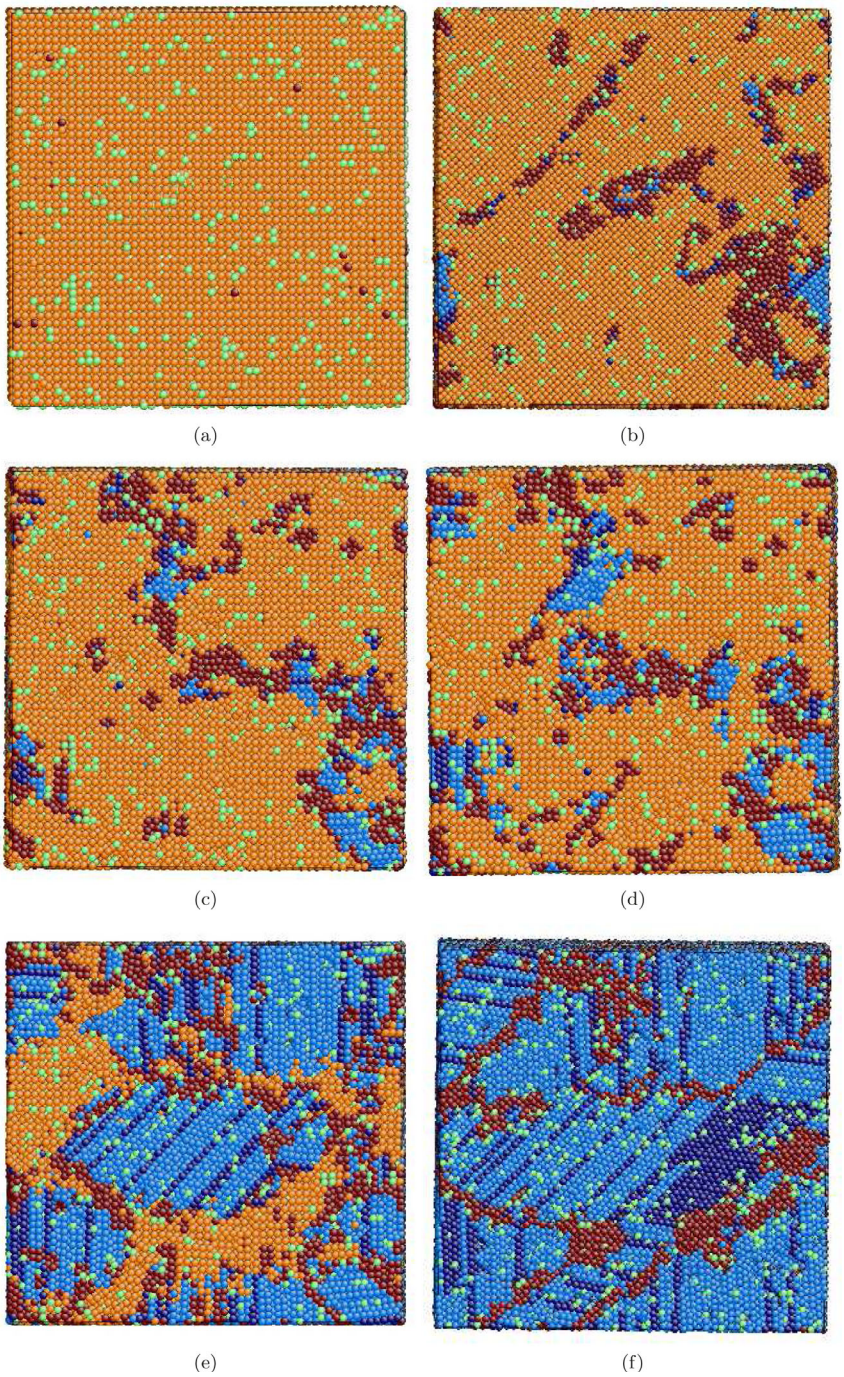

Fig. 5. Snapshots of the $Fe_{1-x}Ni_x$ crystallites (large system) with 10 at% Ni concentration during heating. Temperatures are (a) 0 K, (b) 417 K, (c) 528 K, (d) 564 K, (e) 599 K, (f) 670 K. The plotted plane corresponds to a bcc {100} plane. Colors denote the local crystal structure as in Figure 4.

$x = 10$ at%. According to Figure 3b it occurs at a temperature of around 600 K. Already long before the transformation, at 417 K, small embryos are formed; most of them are not clearly recognizable by the CNA detector and are only rendered as unidentified structures; however, one cp nucleus has clearly formed at this low temperature. The number of nuclei increases with temperature; just before the transformation, at 564 K, at least 5 spatially distinct cp nuclei can be observed. These are of an irregular form and are attached to, or incorporate, unidentified material, which may be in the stage of transforming. The phase transition then occurs very suddenly, and at 599 K, the majority of the material has transformed. Note that since the material has transformed independently at several places, the resulting structure is polycrystalline. After further heating, the remaining bcc material transforms

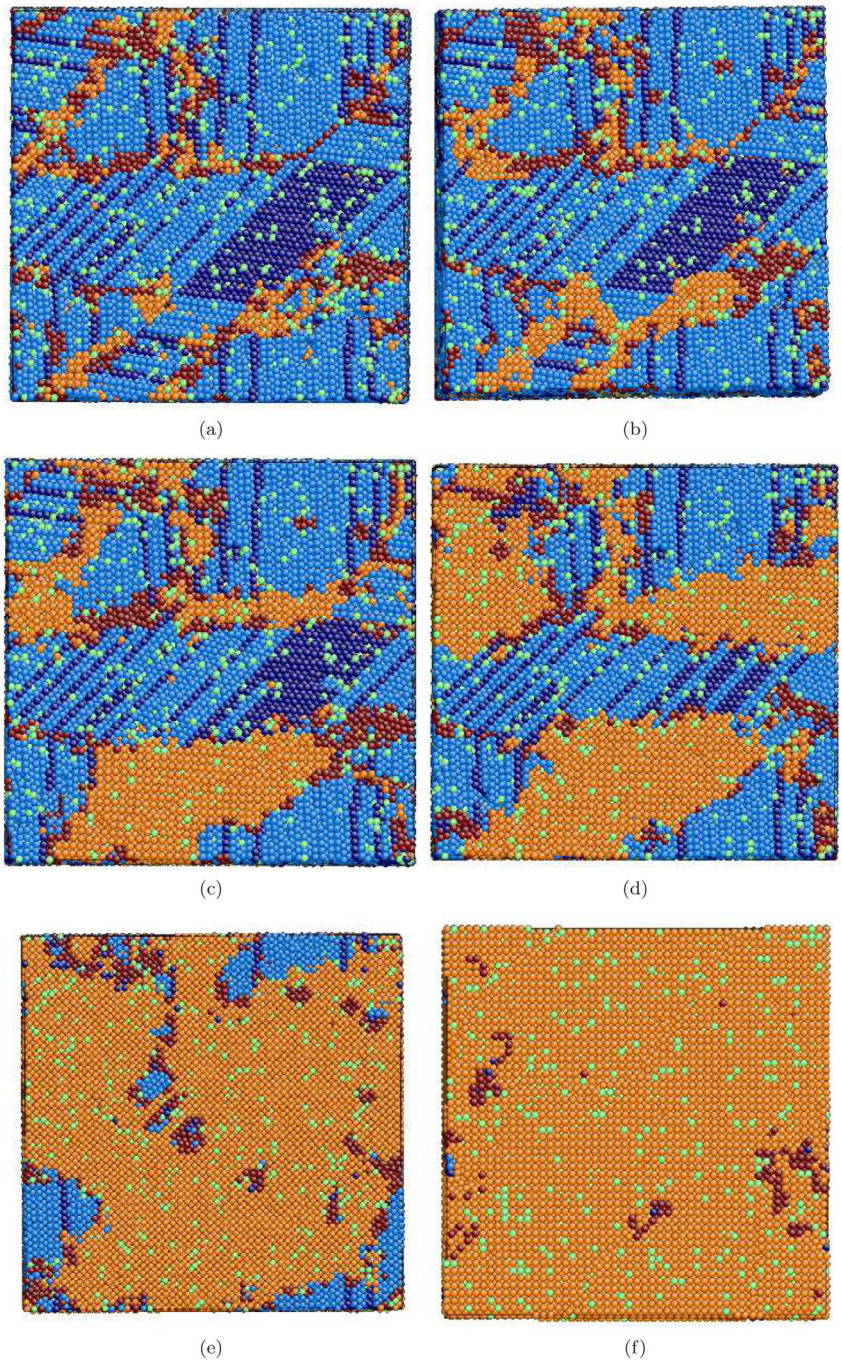

Fig. 6. Snapshots of the $Fe_{1-x}Ni_x$ crystallites (large system) with 10 at% Ni concentration during cooling. Temperatures are (a) 447 K, (b) 378 K, (c) 348 K, (d) 342 K, (e) 321 K, (f) 40 K. The plotted plane corresponds to a bcc {100} plane. Colors denote the local crystal structure as in Figure 4.

and only grain boundaries remain. We conclude that the austenitic transformation follows the path of homogeneous nucleation resulting in a fine-grained structure.

Figure 5e gives a representative example of the microstructure of the fully transformed austenitic phase. It is characterized by the poly-crystalline structure explained above and is thus fundamentally different from the structure of the small system, Figure 4; this fact emphasizes the importance to study sufficiently large systems. In each grain the structure is characterized by a mix of the two close-packed lattice structures, fcc and hcp. Often the fcc phase just appears in the form of stacking fault {111} planes in the hcp material. This feature is characteristic of the austenitic phase transformation of Fe when simulated by the Meyer-Entel potential and has been characterized before both for pure Fe [35–38] and in Fe-C alloys [39].

The martensitic back-transformation is displayed in Figure 6. It occurs, according to Figure 3b, at around

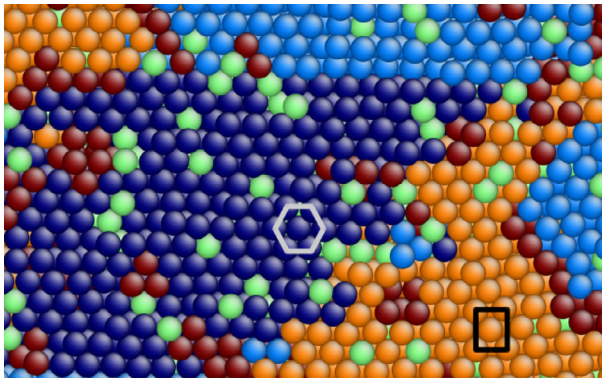

Fig. 7. Close-up view of a $(111)_{\mathrm{fcc}}$ plane transforming into a $(110)_{\mathrm{bcc}}$ plane; the black square and the white hexagon highlight the local crystal structure. The snapshot corresponds to a cross-sectional view of the system displayed in Figure 6c, at 348 K during the martensitic transformation. Colors denote the local crystal structure as in Figure 4.

320 K. In this case the phase transformation starts at the grain boundaries. Note that this occurs already at the temperature of 447 K; however, the transformation proceeds slowly and remains restricted to the grain-boundary material. Between 378 and 348 K, an entire cp grain has transformed, and at 342 K several other grains. Soon after (321 K) almost the entire material has transformed. Thus the martensite transformation starts heterogeneously and transforms grain after grain, apparently independently of each other. This transformation takes more time than the austenite transformation. In the end, finally, an almost defect-free single-crystalline bcc grain has resulted. This may appear surprising. However, it will be shown below (cf. Fig. 7) that the cp phase is created in a simple NW orientation relationship to the original bcc phase; thus during back transformation, the transformed material shows everywhere the same orientation, even though the transformation started from several grains.

The definition of, e.g., martensite *start* and *finish* temperatures is therefore incomplete if not the exact degree of transformation is indicated. However, the main part of the transformation occurs in a quite narrow temperature window. It is this window, which is also seen in Figure 3 as the region where the volume jumps. It may be surmised that pre-existing defects, such as the grain boundaries in the austenitic structure will further broaden the gap between start and finish transformation temperatures.

In the bcc $\rightarrow$ fcc transformation, the dense-packed $\{110\}_{\mathrm{bcc}}$ planes of the bcc phase are transformed into the dense-packed $\{111\}_{\mathrm{fcc}}$ planes of the fcc phase. In the NW orientation relationship, one $[001]_{\mathrm{bcc}}$ axis lying in the plane is left unchanged and transforms to a $[110]_{\mathrm{fcc}}$ axis. This is nicely seen in the transformation plotted in Figure 5, where – even in the dominantly hcp grains – the dark-blue lines indicate the relevant $\{111\}_{\mathrm{fcc}}$ planes. For a detailed discussion note that the plotted plane is the $(001)_{\mathrm{bcc}}$ plane. The cross sections of the transformed $\{111\}_{\mathrm{fcc}}$ planes with the surface run either in diagonal or in vertical direction (see Fig. 5). These two cases are discussed in the following:

(i) In most grains the trace of the transformed $\{111\}_{\mathrm{fcc}}$ planes on the surface lies in diagonal direction. In these grains, the direction perpendicular to the plotted plane, $[001]_{\mathrm{bcc}}$, is left unchanged; this corresponds to a $[110]_{\mathrm{fcc}}$ direction and indicates the orientation of the transformed grains. The diagonal visible is the trace of the $\{110\}_{\mathrm{bcc}}$ plane on the surface that has now become a $\{111\}_{\mathrm{fcc}}$ plane, which runs perpendicular into the material.

(ii) In several grains, the transformed phase features $\{111\}_{\mathrm{fcc}}$ planes whose trace on the surface runs along $[100]_{\mathrm{bcc}}$. This is the invariant direction, which becomes $[110]_{\mathrm{fcc}}$ in the new phase. The pertinent $\{111\}_{\mathrm{fcc}}$ planes run at an oblique angle into the material.

The orientation relationships during the transformation are highlighted in Figure 7.

In Figure 8, we compare the microstructures of phase transformed $\mathrm{Fe}_{1-x}\mathrm{Ni}_x$ alloys with varying Ni content x at the same temperature of 780 K after the austenitic transformation. No clear influence of the Ni content on the structure can be observed; only the number of unidentified atoms (colored red) increases with x since the CNA detector has more difficulties in identifying the local structure in the strained environment around Ni atoms. The microstructure is characterized in all cases by the appearance of both the mixture of hcp and fcc phases discussed above and by the formation of a poly-crystalline structure after transformation.

We determined the phase fraction of the (dominant) hcp phase in the structures of Figure 8. The fraction of Fe atoms in the hcp phase, p_{hcp}, decreases from 0.73 over 0.70 to 0.52 for $x = 0$, 0.1 and 0.3. When normalizing to the total amount of (Fe and Ni) atoms, the normalized fraction $p_{\mathrm{hcp}}/(1-x)$ amounts to 0.73, 078, 074 and thus shows no clear trend as a function of Ni content. We conclude that the presence of Ni does not favor the fcc over the hcp phase, as might have been expected, since pure Ni is fcc.

4 Summary

The Meyer-Entel potential allows us to study the morphological changes in $\mathrm{Fe}_{1-x}\mathrm{Ni}_x$ crystals occurring during the temperature-induced bcc/fcc transformation. In contrast to previous studies of this system, which concentrated on smaller samples of the order of 10^3 atoms, we provide here simulation results for systems containing 2.75×10^5 atoms. The structure obtained by the austenitic transformation is characterized by a fine-grained poly-crystalline structure; it results from the homogeneous nucleation of several competing cp grains in the bcc matrix. We find that the transformation follows the NW orientation relationships. As a result the orientation of the various cp grains are closely related to each other.

The martensitic transformation of this poly-crystalline structure again leads to a single-grained bcc crystal.

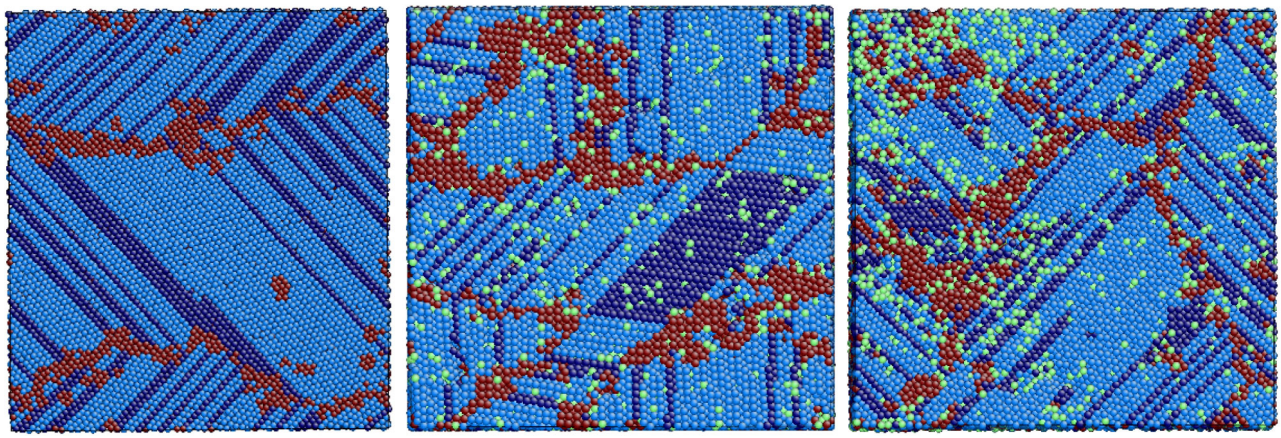

(a) (b) (c)

Fig. 8. Snapshots of (a) pure Fe and of $Fe_{1-x}Ni_x$ crystallites with Ni concentrations of (b) 10 at% and of (c) 30 at% at 780 K after the austenitic transformation. The system had originally a bcc (100) surface. The diagonal fcc lines indicate stacking faults of the {111} planes. Colors denote the local crystal structure as in Figure 4.

This is understandable from the fact that the orientations of the cp grains are related among each other and their transformation thus leads to the same orientation from which they originated. In contrast to the austenitic transformation, the martensitic transformation features heterogeneous nucleation, where the grain boundaries act as nucleation sites. In consequence this transformation also needs a larger temperature window for completion.

The incorporation of Ni into the Fe matrix lowers the austenitic transition temperature, in agreement with experiment. However, we could not observe any significant effect of the Ni concentration x (for $x \leq 30$ at%) on the evolving microstructure nor on the phase fractions of hcp and fcc in the resulting cp phase.

We acknowledge support by the Deutsche Forschungsgemeinschaft via the Sonderforschungsbereich 926.
E.S. and H.M.U. designed the simulation, analyzed the data and wrote the manuscript, and E.S. performed the simulations.

References

1. W. Pepperhoff, M. Acet, *Constitution and Magnetism of Iron and its Alloys* (Springer, Berlin, 2001)
2. M. Acet, T. Schneider, E.F. Wassermann, J. Phys. IV France **05**, C2-105 (1995)
3. Z.-Z. Yu, P.C. Clapp, Metall. Trans. A **20**, 1617 (1989)
4. M. Grujicic, P. Dang, Mat. Sci. Eng. A **201**, 194 (1995)
5. M. Grujicic, S.G. Lai, P. Gumbsch, Mat. Sci. Eng. A **231**, 151 (1997)
6. G.V. Kurdjumov, G. Sachs, Z. Phys. **64**, 325 (1930)
7. Z. Nishiyama, Sci. Rep. Tohoku Imp. Univ. **23**, 637 (1934)
8. G. Wassermann, Arch. Eisenhüttenwes. **6**, 347 (1933)
9. R. Meyer, P. Entel, Phys. Rev. B **57**, 5140 (1998)
10. R. Meyer, P. Entel, J. Phys. IV France **05**, C2-123 (1995)
11. R. Meyer, P. Entel, J. Phys. IV France **07**, C5-29 (1997)
12. R. Meyer, K. Kadau, P. Entel, in *Properties of Complex Inorganic Solids*, edited by A. Gonis, A. Meike, P.E.A. Turchi (Plenum, New York, 1997), p. 95
13. K. Kadau, P. Entel, P.S. Lomdahl, Comput. Phys. Commun. **147**, 126 (2002)
14. K. Kadau, P. Entel, Phase Trans. **75**, 59 (2002)
15. P. Entel, M. Kreth, R. Meyer, K. Kadau, in *Modeling and Simulating Materials Nanoworld*, Advances in Science and Technology, edited by P. Vincenzini, F. Zerbetto (Techna Group, Faenza, 2004), Vol. 44, p. 101
16. L.E. Kar'kina, I.N. Kar'kin, Y.N. Gornostyrev, Phys. Met. Metallogr. **101**, 130 (2006)
17. G. Bonny, R.C. Pasianot, L. Malerba, Model. Simul. Mater. Sci. Eng. **17**, 025010 (2009)
18. Y. Mishin, M.J. Mehl, D.A. Papaconstantopoulos, Acta Mater. **53**, 4029 (2005)
19. L. Malerba et al., J. Nucl. Mater. **406**, 7 (2010)
20. P. Entel, R. Meyer, K. Kadau, H.C. Herper, E. Hoffmann, Eur. Phys. J. B **5**, 379 (1998)
21. P. Entel, K. Kadau, R. Meyer, V. Crisan, H. Ebert, T.C. Germann, P.S. Lomdahl, B.L. Holian, Adv. Solid State Phys. **40**, 345 (2000)
22. P. Entel, R. Meyer, K. Kadau, Philos. Mag. B **80**, 183 (2000)
23. S. Plimpton, J. Comput. Phys. **117**, 1 (1995)
24. D. Faken, H. Jonsson, Comput. Mater. Sci. **2**, 279 (1994)
25. C. Kittel, *Introduction to Solid State Physics*, 8th edn. (Wiley, 2005)
26. N. Saunders, A.P. Miodownik, A.T. Dinsdale, Calphad **12**, 351 (1988)
27. M.I. Baskes, Mater. Chem. Phys. **50**, 152 (1997)
28. E.A. Owen, E.L. Yates, A.H. Sully, Proc. Phys. Soc. **49**, 315 (1937)
29. L. Zwell, D.E. Carnahan, G.R. Speich, Metall. Trans. **1**, 1007 (1970)
30. E. Jartych, J.K. Zurawicz, D. Oleszak, M. Pekala, J. Magn. Magn. Mater. **208**, 221 (2000)

31. N.P. Lazarev, C. Abromeit, R. Schäublin, R. Gotthardt, J. Appl. Phys. **100**, 63520 (2006)
32. V.G. Sathe, S. Banik, A. Dubey, S.R. Barman, A.M. Awasthi, L. Olivi, Adv. Mater. Res. **52**, 175 (2008)
33. C. Engin, L. Sandoval, H.M. Urbassek, Model. Simul. Mater. Sci. Eng. **16**, 035005 (2008)
34. L. Sandoval, H.M. Urbassek, P. Entel, Phys. Rev. B **80**, 214108 (2009)
35. B. Wang, H.M. Urbassek, Phys. Rev. B **87**, 104108 (2013)
36. B. Wang, H.M. Urbassek, Acta Mater. **61**, 5979 (2013)
37. B. Wang, H.M. Urbassek, Model. Simul. Mater. Sci. Eng. **21**, 085007 (2013)
38. B. Wang, H.M. Urbassek, Comput. Mater. Sci. **81**, 170 (2014)
39. B. Wang, E. Sak-Saracino, N. Gunkelmann, H.M. Urbassek, Comput. Mater. Sci. **82**, 399 (2014)